Bulletin of the Mineral Research and Exploration

http://bulletin.mta.gov.tr

Investigation of the relationship between Remote Sensing and Ground Observations in the detection of hematite minerals in Vera Rubin Ridge, Mars

Mehmet Ali AKGÜL[*a,b] and Suphi URAL[c]

[a] *General Directorate of State Hydraulic Works, 6Th Regional Directorate, Department of Information Technologies, Geographic Information Systems Section, Adana, Türkiye*

[b] *Çukurova University, Institute of Natural and Applied Sciences, Department of Remote Sensing and Geographic Information Systems, Adana, Türkiye*

[c] *Çukurova University, Department of Mining Engineering, Adana, Türkiye*

Research Article

Keywords: Astrogeology, Hyperspectral Remote Sensing, Hematite, Vera Rubin Ridge.

ABSTRACT

The sensors on landers and rovers on Mars enable the performance of highly sensitive analyses in a limited area. However, orbiting satellites can observe the entire surface of Mars, albeit with coarser results than those obtained by landers and rovers. The objective of the study was to calibrate the distribution of hematite (Fe_2O_3) minerals derived from satellite data using ground observations, thereby producing more sensitive data across a larger area of the Vera Rubin Ridge (VRR) region. This topographic elevation extends from the northeast to the southwest in the northwest region of the Gale Crater. In the study, a model was established between the CRISM instrument data on the MRO satellite and the Mastcam sensor data on the Curiosity rover to determine the corrections that should be applied to the satellite data. The BD860_2 parameter, which identifies the hematite mineral, was adjusted to ModBD860_2 by employing the model's regression coefficients, which exhibited a Pearson correlation coefficient (r) of 66% and a mean absolute error (MAE) of 2.1%. By applying the ModBD860_2 indice to the CRISM data, it was concluded that areas where the BD860_2 indice did not detect the presence of hematite could also be potential exploration areas.

Received Date: 06.09.2024
Accepted Date: 14.05.2025

1. Introduction

Gale Crater was selected as the landing site for the Curiosity Rover because satellite data indicated the presence of minerals indicative of aqueous processes, such as phyllosilicates and iron oxides (Grotzinger et al., 2012; Milliken et al., 2010), as well as the diversity of potentially habitable geological environments in the ancient layered sedimentary rocks that form the lower slopes of Aeolis Mons (Golombek et al., 2012). Gale Crater, an impact crater with a diameter of 155 km located in the crustal dichotomy of Mars, has some of the lowest altitudes in the southern hemisphere (Wray, 2013). The sedimentological investigations conducted on the basis of the images captured by the Curiosity rover have revealed that the Gale Crater was once home to an ancient fluviolacustrine ecosystem (Grotzinger et al., 2014, 2015). Additionally, visible/short wave infrared (VSWIR) reflection spectra obtained by Compact Reconnaissance Imaging Spectrometer for Mars (CRISM) from the lower portions of Aeolis Mons indicate the presence of diverse units comprising minerals that may have been formed through aqueous alteration, including

Citation Info: Mehmet Ali Akgül, M. A., Ural, S. 2025. Investigation of the relationship between Remote Sensing and Ground Observations in the detection of hematite minerals in Vera Rubin Ridge, Mars. ulletin of the Mineral Research and Exploration 177, 23-41. https://doi.org/10.19111/bulletinofmre.1699049

**Corresponding author: Mehmet Ali AKGÜL, mali.akgul@dsi.gov.tr*

hematite, smectite, and sulfates (Milliken et al., 2010, Fraeman et al., 2013, 2016). One of the main areas of interest during Curiosity's exploration of Aeolis Mons was the Vera Rubin Ridge (VRR) region, about 6.5 km long and 200 m wide, at an altitude of about 10 m from its surroundings. CRISM spectra of the VRR region, a topographic elevation on the northwest flank of Aeolis Mons and running northeast-southwest, shows pixels consistent with crystalline hematite with absorption properties close to 0.55 and 0.86 μm (Fraeman et al., 2013, 2016). The presence and diversity of crystalline hematite may be due to a warmer more humid climate, very different from the cold, dry climate present on Mars, where it may have originated from oxidized lake waters in the Gale Crater (Hurowitz et al., 2017; Rampe et al., 2017).

Buz et al. (2017) identified various lithologies in the non-bedrock and sediment units at the base of the Gale Crater, which were interpreted to have been transported from the slopes. In the results of their analysis using the images of the Thermal Emission Imaging System (THEMIS) and CRISM sensors, they did not observe significant differences in the spectral properties of the bedrock, but in some CRISM images of the rocks on the slopes, they observed olivine-containing bedrock accompanied with Fe/Mg phyllosilicates. They speculated that the spectral properties of these phyllosilicates were different from the Aluminum-substituted nontronite detected by CRISM at Mount Sharp; therefore, they were formed by liquids of different compositions.

Based on the detection of hematite in VRR by CRISM and the absence of similar strong absorptions in layers immediately adjacent to the ridge, Fraeman et al. (2013) hypothesized that the VRR might be a unique, hematite-rich range marking the localized region of iron oxidation and the potential past habitable environment. Understanding the formation environments for the hematite-rich ridge is important for its implications for the wider Martian paleo-environment context, particularly in the Gale Crater (Fraeman et al., 2020).

A comprehensive understanding of the planets paleoclimate necessitates the precise delineation of the mineral assemblage present in Martian rocks. However, this may prove challenging when orbital spectral data represent the sole accessible source of information. In particular, some minerals with bright visible colors, such as hematite, can mask the presence of iron phyllosilicate-like minerals by suppressing the spectral signal (Jacob et al., 2020). CheMin on the Curiosity rover observed crystalline hematite in the VRR bedrock (Rampe et al., 2020), thereby corroborating the CRISM data's conclusion that VRR includes hematite. The CRISM-based interpretation that the VRR is a unique hematite-bearing region in Aeolis Mons is therefore incorrect. However, the bedrock regions of interest (ROIs) from lower elevations of Aeolis Mons analyzed by CheMin do contain hematite, but these areas do not show strong hematite absorptions in the CRISM data. Quantitative XRD measurements from Curiosity's CheMin instrument facilitated the identification of significantly greater quantities of ferrous phyllosilicates than would have been anticipated based on orbital data. Additionally, the presence of minor amounts of iron minerals, including jarosite and akaganeite, was discerned, which had not been predicted by satellite data (Rampe et al., 2017, 2020; Bristow et al., 2018).

The CRISM data will continue to help the rover as it ascends Aeolis Mons and passes through stratigraphic units with orbital spectrum signatures compatible with phyllosilicates and sulfates. These findings may point to the presence of changing Martian habitats (Milliken et al., 2010). CRISM data will be used for strategic route planning to locate and access critical rocks/minerals by NASA's Mars rovers and ESA's ExoMars rover, which is scheduled to be sent to Mars in 2028 (ESA, 2025).

Horgan et al. (2020) utilized the Mastcam and ChemCam sensors on the Curiosity rover to ascertain the mineralogical origins of the extensive range of color variations, spanning from red to purple and gray, in the VRR region. The researchers hypothesized that these color variations are most likely the result of diagenetic changes in the sediments after deposition. Understanding the influence of these events on the chemical and mineralogical properties of ancient Martian habitats is critical to understanding the past habitability of the planet.

Three drilled samples were successfully obtained on VRR, one in the Blunts Point (Duluth, DU) and Pettegrove Point (Stoer, ST) members, and two in the Jura member (Highfield, HF; Rock Hall, RH). The successfully drilled samples were investigated using CheMin, which revealed a variety of secondary minerals relevant to the spectrum analyses in this work (Rampe et al., 2020). These included crystalline hematite, with abundances of 6.1% in the DU sample, 14.7% in the ST sample, 8.5% in the HF sample, and 2.9% in the RH sample (where abundances are represented as weight percentages of the bulk sample). The targets at Blunts Point are characterized by the presence of resistant veins in the bedrock, while the presence of scratches in the bedrock indicates that it is poorly cemented and contains numerous veins that obscure bedding features. The bedrock is typically red, and the most prevalent diagenetic features are nodules and dark-toned facies. Pettegrove Point targets generally have two different appearances: continuous lamination or a high concentration of nodules obscuring the lamination. The Pettegrove Point target ranges from brown to red to purple with red being the most common color. The lighter veins at Pettegrove Point are also recessive to the host rock. These observations suggest that the Pettegrove Point member rocks are probably harder or better cemented than the Blunts Point member rocks. The average estimated grain size of the Pettegrove Point targets is in the mudstone range, but individual targets range in grain size from very fine sand to medium sand. There are two distinct categories of targets within the Jura member: red and gray. Red Jura targets occur as zones of rock that are highly fractured and not clearly visible. Red Jura targets lack nodules and exhibit maximum lamination density. At the same time, the red Jura material lacks scratch marks. The red Jura rocks have characteristics that indicate they are harder than those in the Blunts Point member. On the other hand, the gray Jura targets have a distinct gray color and various diagenetic features. Dark gray features are common in the Gray Jura targets, while prismatic features are observed only in these targets. The Gray Jura rocks also appear to be harder than those in the Blunts Point member. The gray Jura targets have slightly larger grain sizes than the red Jura targets (Bennett et al., 2021).

Bennett et al. (2021) explored the color, grain texture, and lamination style of bedrock, as well as the nodules, diagenetic crystals, and various dark gray iron-rich features in the VRR region using the MAHLI sensor on the Curiosity rover. The results of their study revealed abundant and widespread diagenetic features in the rocks remaining in the VRR region, indicating that the rock targets estimated to be coarser generally had finer grains, had more diagenetic features than predicted, and this would have affected the degree and type of diagenesis of grain size.

Rice et al. (2022) created a database of Mastcam spectra from more than 600 multispectral observations, revealing nine rock and five soil spectral classes. They found that the rock classes are dominated by hematite and oxides, while the soil classes are dominated by fine-grained Fe-oxides and olivine-bearing sands. The soil spectra were influenced by dark, mafic sands from the active Bagnold Dune area, rather than sediments found in the area.

Eng et al. (2024) utilized Mastcam spectra in conjunction with chemical data from the CheMin, APXS, and ChemCam instruments on the Curiosity rover to assess the variability of rock spectra at the clay-sulfate transition and surrounding regions and to interpret mineralogy and diagenesis in Gale Crater. In their study, they also measured the spectral response of mixtures containing phyllosilicates, hydrated Mg-sulfate, and basalt in the laboratory to determine the Mg-sulfate detection capabilities of Mastcam and to aid in the analysis of multispectral data. Their findings revealed that hydrated Mg-sulfates were readily obscured by other constituents, necessitating ≥90 wt% hydrated Mg-sulfate to manifest a discernible hydration signature in Mastcam spectra.

Turner and Lewis (2023) investigated the bedding geometries of exposed bedrock along a traverse on Mount Sharp, and found that bedding typically ranged from 2 to 5° from horizontal and extended radially outward from the center of the mound. The researchers employed in situ Mastcam and Navcam stereo topographic data from the Curiosity rover, in conjunction with long-baseline Mastcam stereo and orbital stereo techniques, to ascertain the structural configuration of bedding planes on Mount Sharp.

Fraeman et al. (2020) stated in their study that the results obtained from CRISM data can be validated with surface property information obtained from in situ observations. They stated that the presence of hematite in the VRR region, as predicted by CRISM, was confirmed by Curiosity and that the accuracy of mineral identifications based on spectral absorptions imaged from orbit can be trusted. They also noted that by using Curiosity's discoveries in the VRR, CRISM can predict regions beyond a narrow path with much greater confidence, with information on surface properties derived from in situ observations. The current results from Gale Crater are promising for future exploration strategies based on a combination of orbital and in-situ spectral observations.

Although landers and rovers on the surface of Mars can perform very precise analyses with the sensors on them, they can only work in a limited area, while satellites in orbit can observe the entire surface of Mars, but can analyze with coarser results than landers/rovers. Unlike landers, which can perform point analysis, rovers can move and analyze more areas, but these areas are very limited when considering a whole planet. The main objective of this study is to establish a model to increase the accuracy of satellite data using in situ data.

The hematite mineral, which is sensitive to 860 nm band depth in CRISM data and 867 nm band depth in Mastcam sensor, was detected using both CRISM and Mastcam sensors on the northwest flank of Aeolis Mons and in the VRR region of a topographic elevation extending in the northeast-southwest direction. The application of the algorithm developed in this study to CRISM data has led to the conclusion that regions where satellite data is unable to detect the presence of hematite with current techniques can also be considered potential research areas. Furthermore, it has been determined that the use of corrected CRISM data in route planning to locate significant minerals such as hematite in future exploration vehicle missions would be more accurate.

The second objective of this study is to examine the members of the VRR region in detail to determine the implications for the interpretation of reflection data of hematite minerals that can be correlated with mineral abundances derived from Mastcam and CRISM data. The VRR region has three different members: Blunts Point (BP), Pettegrove Point (PP), and Jura (JR). The correlation between the CRISM pixels corresponding to each member and the Mastcam ROIs was analyzed. The objective of this analysis is to ascertain which member(s) can be detected with greater accuracy and precision in the production of satellite-based mineral distribution maps.

2. Study Area and Data

This section is divided into three subsections. The first subsection provides a comprehensive explanation of the geographical location, geology, and stratigraphy of the VRR region on Mars. The second subsection details the CRISM instrument on the Mars Reconnaissance Orbiter (MRO) satellite, which was utilized to obtain the remote sensing data for the study. The third subsection delves into the features of the Mastcam sensor on the Curiosity Rover, which provided the ground observation data for the study.

2.1. Study Area

The study area is the region called the upper Gediz Valley of Gale Crater, which is approximately 155 km in diameter and where the Curiosity rover landed at 4.5895°S, 137.4417°E coordinates according to the Mars coordinate system (Vasavada et al., 2014). In the center of the crater is Mount Aeolis Mons, which is approximately 5.5 km above the base (Figure 1). The Curiosity rover successfully landed in this region on 08/06/2012 and is still continuing its mission.

The geological history of Mars has been divided into three periods, Noachian, Hesperian, and Amazonian, from ancient times to the present, through studies of impact crater densities on the Martian surface (Tanaka et al., 2014). Acidic weathering conditions during the Hesperian period resulted in the enrichment of sulfates in layered deposits within Valles Marineris and Gale Crater (Hesperian transition undivided unit, Htu) and in Schiaparelli, Terby, and other highland craters (Hesperian and Noachian highland undivided unit, HNhu) (Bibring et al., 2006).

This period is notable for significant erosion of geologic terrains on Mars. The Amazonian period,

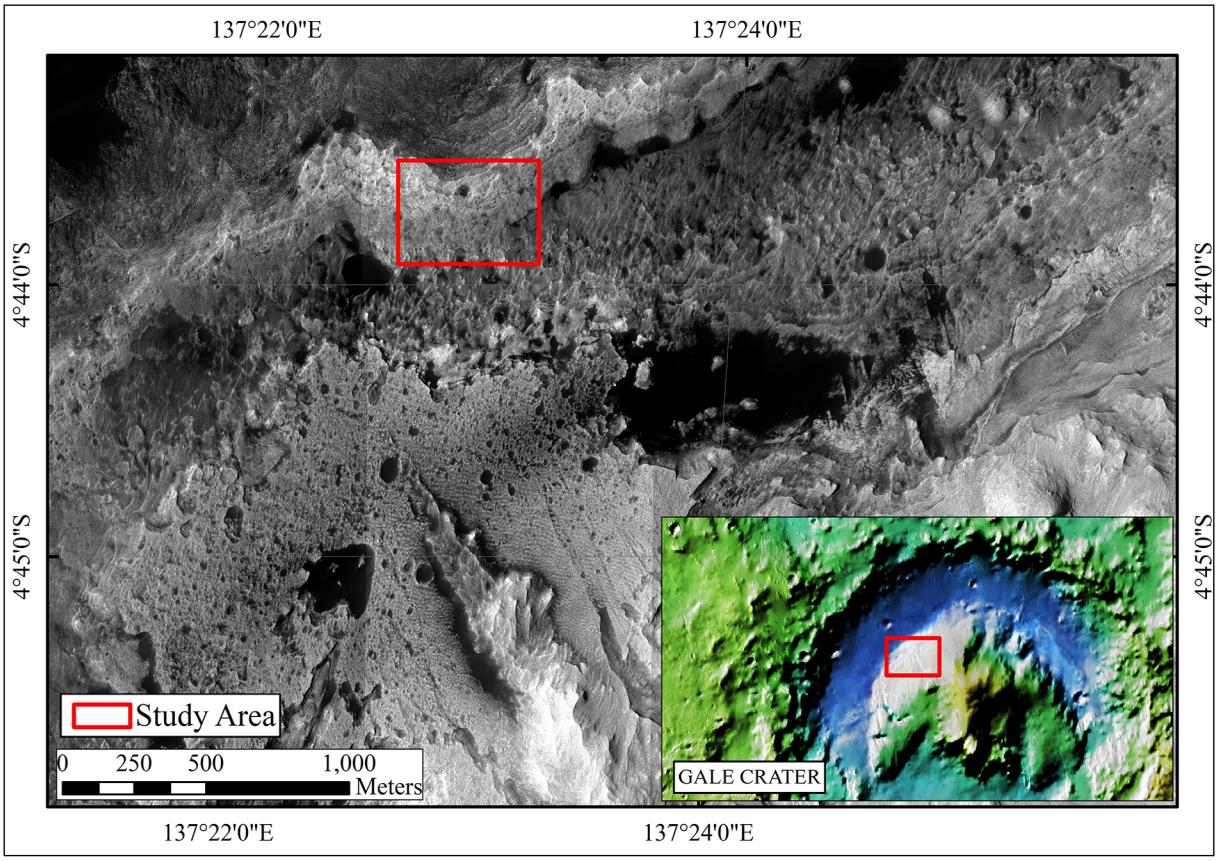

Figure 1- Study area (Akgül and Ural, 2022).

while the longest geological period for Mars, was characterized by a cold, dry, and oxidizing environment, reduced global impact fluxes, and intermittent volcanism (Hartmann and Neukum, 2001; Grant and Wilson, 2011). Fluvial and glacial activity during this period exhibited significantly reduced rates of material deposition and cumulative amounts of geologic modification compared to previous periods (Golombek et al., 2006).

The geological structure of the Gale Crater, on the other hand, covers the period from the border of the Noachian-Hesperian period, called the AHi unit (Amazonian and Hesperian impact unit), to the Amazonian period (Figure 2). Iron oxides are the most prevalent minerals in the Late Hesperian and Amazonian periods. The environment became increasingly arid and cold towards the end of the early Hesperian epoch, as the Martian atmosphere thinned and surface water levels declined. This trend has continued until the present day. Peroxides from the atmosphere oxidized the iron-rich rocks, which represents a significant geological process. During this period, the production of iron oxides was likely to have been extensive, with minerals linked with liquid water being enriched in the Noachian and Hesperian geological units (Bibring et al., 2007; Xue and Jin, 2014).

The traverse of the Mount Sharp group by the rover has maintained Curiosity within the Murray formation, a package of predominantly lacustrine mudstone with uncommon intercalated cross-stratified sandstones of prodeltaic, fluvial, or eolian origin (Grotzinger et al., 2015; Rivera-Hernandez et al., 2020). The Murray formation, with a thickness of at least 300 m, is divided into seven different members, namely the Pahrump Hills member, Hartmann's Valley member, the Karasburg member, the Sutton Island member, the BP member, the PP member, and the JR member, and its stratigraphic column is shown in Figure 3 (Stein et al., 2020). The members of PP, JR, and BP comprise the VRR region, which we are studying. The Pahrump Hills member is made up of thin layers of mudstone

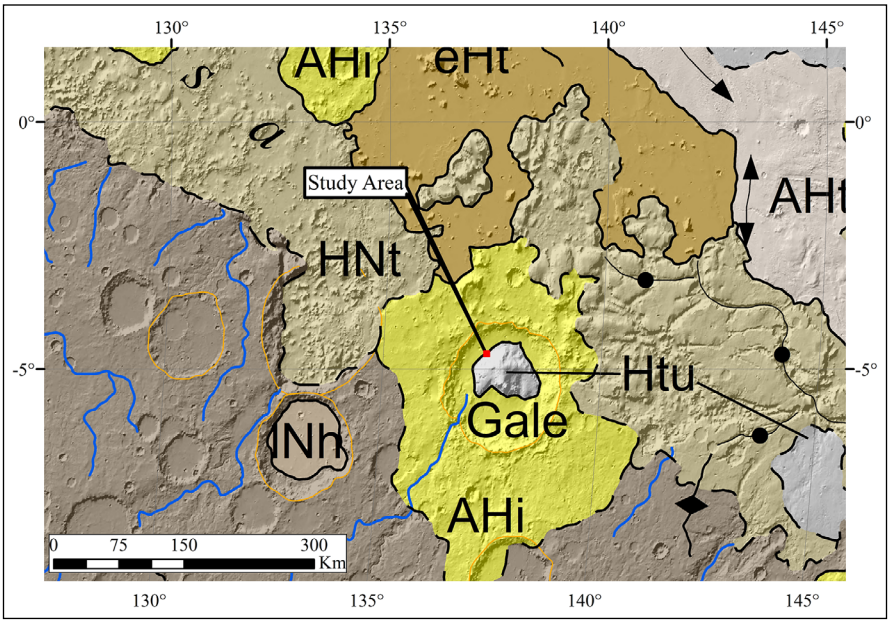

Figure 2- Geological map of the study area (Tanaka et al., 2014).

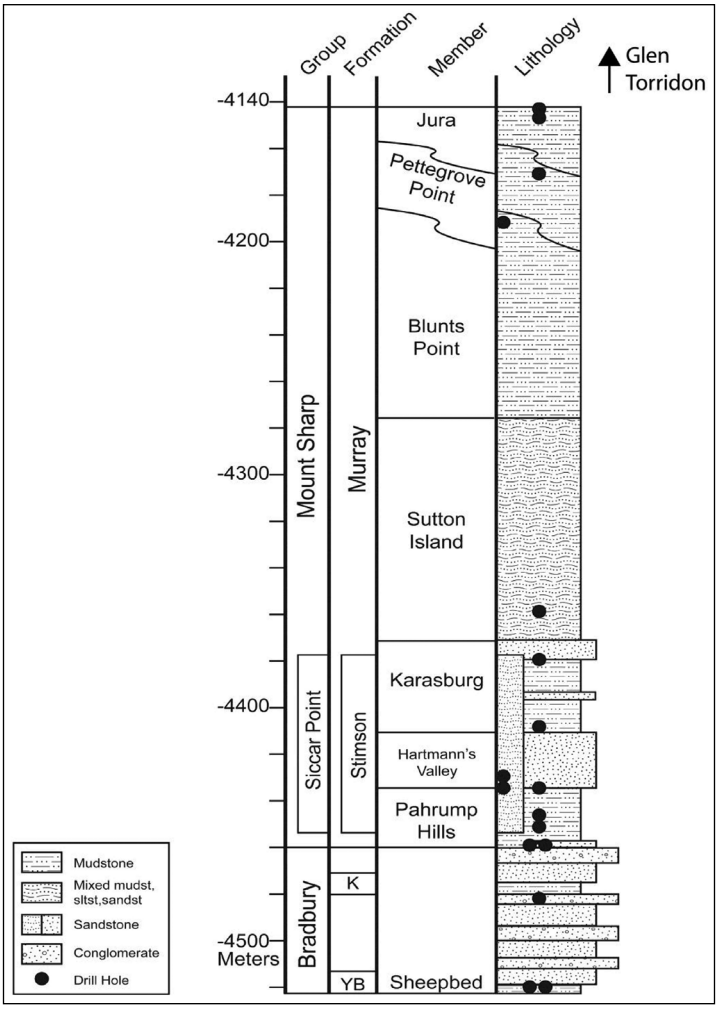

Figure 3- Stratigraphic column along Curiosity's traverse (Stein et al., 2020).

that were probably deposited by strong flows of water in a lake (Grotzinger et al., 2015; Stack et al., 2019). The Hartmann's Valley member is made up of layers that are between decimeters and meters thick. These layers show signs of being shaped by wind or water (Fedo et al., 2018; Gwizd et al., 2019). The Sutton Island member is a mudstone-sandstone that's mostly made of broken meter-scale blocks. It has signs of dry conditions that happened regularly, like desiccation cracks and sulfate enrichments (Rapin et al., 2019; Stein et al., 2018).

The BP member, a fine-grained recessive facies with widespread planar lamination and copious calcium sulfate veins, correlates with the base of the higher north-facing cliff of the VRR (Fedo et al., 2019; Edgar et al., 2020). The PP member is stratigraphically superior to the BP member, exhibiting precipitous cliffs at the summit of the ridge's northern side. In terms of physical characteristics, the PP member is similar to the BP member. However, it exhibits more pronounced diagenetic traits, a reduction in sulfate veins, and enhanced resistance to erosion (Tinker et al., 2019; Edgar et al., 2020; Bennett et al., 2021). The PP member is overlain by the JR member, which together constitute the summit of the ridge. The JR component remains tightly laminated, yet displays considerably greater variation in color, texture, and sedimentary structures than the PP or BP members (Bennett et al., 2021). The contact between the PP and JR components is distinguished by a noticeable step in topography, corresponding to large-scale inclined beds, and a distinct facies defined by alternating thinly and densely laminated packages of mudstone to fine sandstone (Edgar et al., 2020). Figure 4 shows the boundaries of the VRR region for the BP, PP, and JR members.

2.2. CRISM Data

The CRISM instrument on the MRO satellite is a hyperspectral imaging spectrometer designed to map the surface mineralogy of Mars (Murchie et al., 2007).

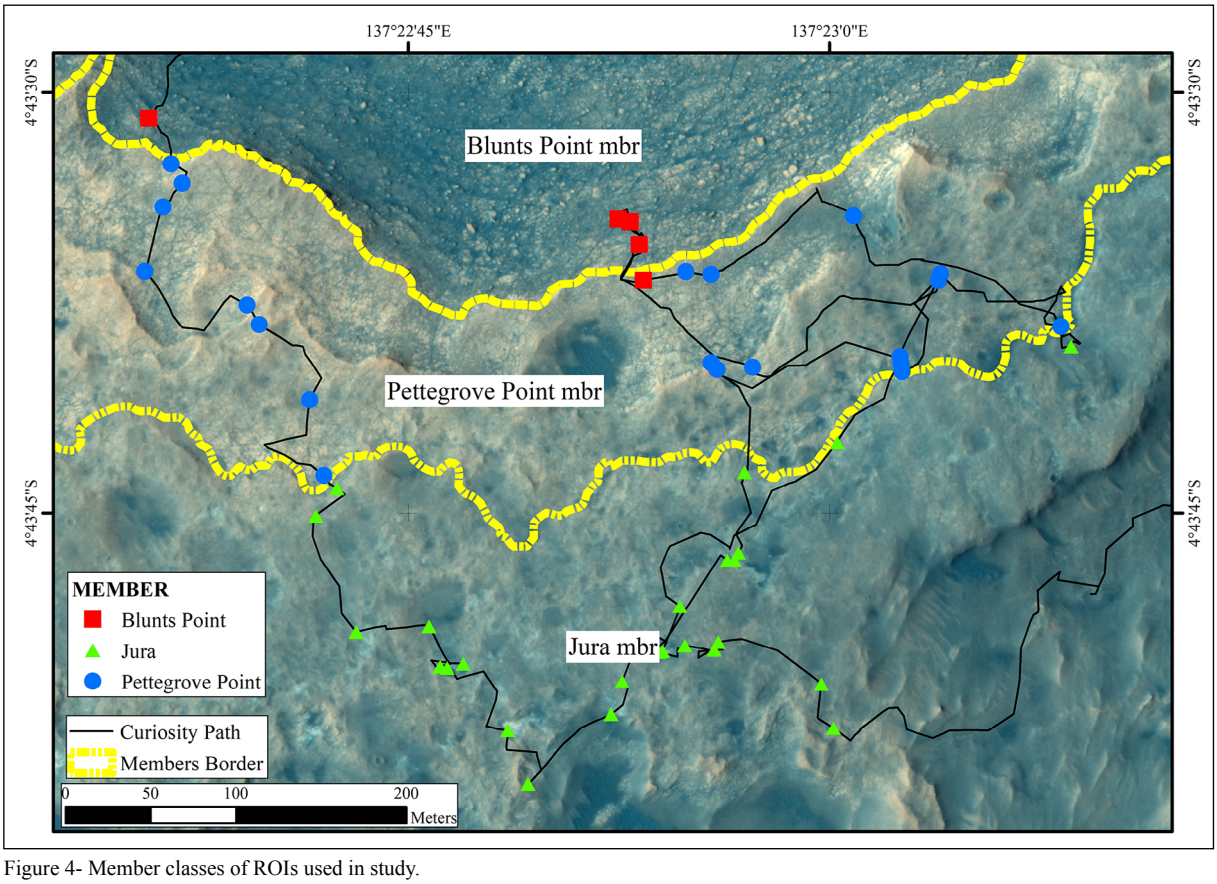

Figure 4- Member classes of ROIs used in study.

The sensor is specifically designed to look for evidence of hydrothermal deposits and other mineralogical indicators of water. This satellite was launched from the Cape Canaveral space base in the United States on 12.08.2005 and entered Mars orbit on 10.03.2006.

CRISM images the Martian surface and atmosphere in two different modes: mapping mode and targeted mode. In targeted mode, CRISM targets a location and uses its gimbal to take multiple images along a line. These images are then combined to create a single image of the target. The instrument's gimbal tracks a point on the surface and scans an area of about 10 km x 10 km at about 18 meters per pixel and 545 wavelengths. In mapping mode, CRISM collects data to take long swaths of images. In this mode, it collects data at 5 to 10 times lower resolution and fewer wavelengths (between 72 and 262) than in targeted mode to produce a global map of Mars (Seelos et al., 2024). CRISM observation modes, spatial resolutions, and number of bands are shown in Table 1.

Table 1- CRISM observing modes (Morgan et al., 2017).

Mode	Spatial Res. (m/pix)	Mapping/ Targeted	Number of Bands	
			VNIR	IR
MSP	~200	M	19	55
MSW	~100	M	19	55
HSP	~200	M	107	154
HSV	~200	M	107	N/A
MSV	~100	M	90	N/A
FRT	~20	T	107	438
HRL	~40	T	107	438
HRS	~40	T	107	438
ATO	~20x10	T	107	438
FRS	~20	T	107	438
ATU	~20x40	T	107	438
MSP	~200	M	19	55

The image "FRT0000B6F1" corresponding to the working area of the CRISM sensor was taken from the Planetary Data System (https://ode.rsl.wustl.edu/mars/) site (Figure 5). This data is a hyperspectral

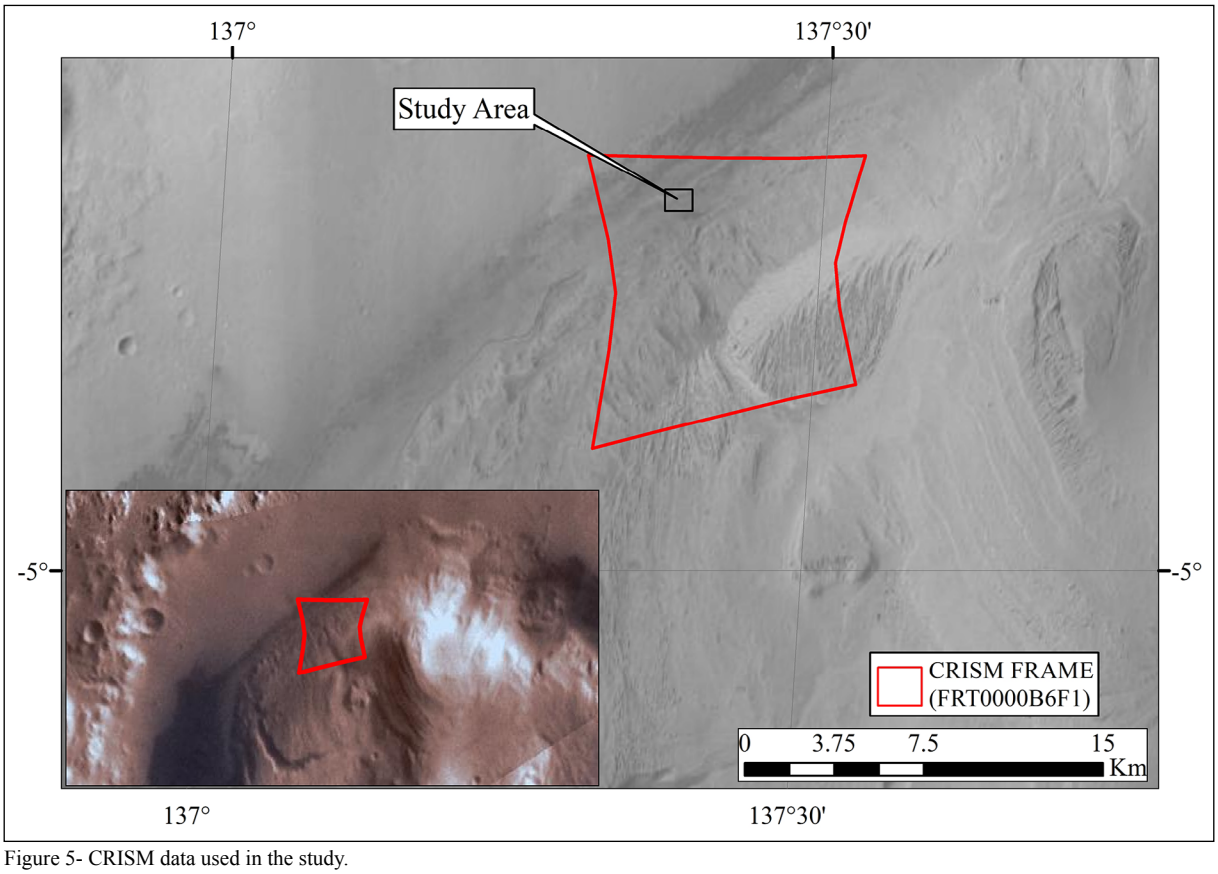

Figure 5- CRISM data used in the study.

image with 545 bands between 0.36 μm and 3.92 μm and has a spatial resolution of 18 meters. 544 bands are used in the analysis of the hyperspectral CRISM image, and there is an extra line from the IR detector to measure the electronic background (Murchie et al., 2007).

2.3. Ground Observation Data

The Curiosity Rover, which was launched from the Cape Canaveral space base with the Atlas V 541 rocket on 26.11.2011 and successfully landed in the Gale Crater region on 06.08.2012, has been in service since 22.8.2012. Many advanced sensors are available on this rover. The Mastcam sensor used in the study consists of two cameras on a fixed and vertical mast on the Curiosity rover, the electronics inside the rover, and a calibration target on the body of the rover. The two cameras of the Mastcam sensor are positioned at a height of about 2 m from the ground, considering the height of the human eye, and it is possible to obtain stereoscopic images with a distance of 24.64 cm between them. The right camera can take images 3 times more sensitive than the left camera, and this sensitivity corresponds to 7.4 cm at a distance of 1 km. The left camera can view a wider area than the right camera. With Mastcam, the geomorphology, stratigraphy and texture of the landscape, rocks and sediments around the rover can be investigated. It is also possible to monitor atmospheric and even astronomical events. The wavelengths and properties of the bands of Mastcam cameras are given in Table 2.

Table 2- Mastcam sensor band specification (Bell et al., 2017).

Filtre	Mastcam-L (nm)	Filtre	Mastcam-R (nm)
L0 (Red)	640 ± 44	R0 (Red)	638 ± 44
L0 (Green)	554 ± 38	R0 (Green)	551 ±39
L0 (Blue)	495 ± 37	R0 (Blue)	493 ±38
L1	527 ±7	R1	527 ± 7
L2	445 ±10	R2	447 ± 10
L3	751 ± 10	R3	805 ± 10
L4	676 ± 10	R4	908 ± 10
L5	867 ± 10	R5	937 ± 10
L6	1012 ± 21	R6	1013 ± 21

3. Methodology

The Methodology section is divided into three subsections. The first subsection is the CRISM data processing for mineral analysis subsection, which expounds on the methodology of performing mineral analysis with CRISM data utilized as remote sensing data in the study. The second subsection is the Ground observations data processing for mineral analysis subsection, which details the process of conducting mineral analysis with the Mastcam sensor. The third subsection is the Relationship between Ground observations and remote sensing subsection, which elucidates the relationship between ground observations and remote sensing.

3.1. CRISM Data Processing for Mineral Analysis

CRISM Analysis Software (CRISM Analysis Toolkit, CAT) is a software system that runs on the IDL/ENVI program to analyze and display data from the CRISM detector. CAT works as an ENVI program add-on, so ENVI's built-in imaging and spectral analysis tools are available after CRISM data has been loaded and processed. (Morgan et al., 2017). In the study, the CRISM data were analysed using CAT software, and the workflow diagram we created for this analysis is shown in Figure 6.

The photometric correction is performed by dividing the CRISM image by the cosine of the solar incidence angle, while the atmospheric correction is performed by eliminating all CO_2 absorption bands with a scaled atmospheric transmission spectrum

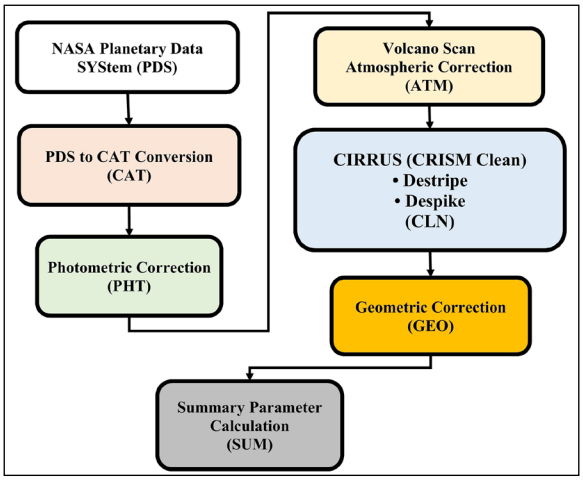

Figure 6- CRISM data analysis flowchart.

obtained during an observation over Mount Olympus Mons. This is done using the spectrum difference measured from the summit and base of the highest mountain in our Solar system, and thus Mars. While the noise on the image is corrected with data filtering, the reconstruction of missing pixels with the average of the surrounding pixels is done with Line correction. Photometric, atmospheric, and data filtering/line -corrected images must be defined in a projection system to use them in a coordinated manner. This correction is made with a Geometric correction (Gurunadham and Kumar, 2014; Arvidson et al., 2017). Indices shown as SUM in Figure 6 were calculated using the corrected CRISM data, using the CAT software for which the corrections were made. The majority of these indices are indices that calculate the Band Depth (BD). BD is one of the most widely used methods for parameterizing spectral data (Clark and Roush, 1984). The BD860_2 indice, which calculates the band depth at 860 nm where hematite is absorbed in CRISM data, is calculated as given in Equation 1 and described in Viviano-Beck et al. (2014). In Equation 1, the (a) value is 0.527 and the (b) value is 0.473.

$$BD860\_2 = 1 - \left(\frac{R_{860}}{a * R_{755} + b * R_{977}}\right) \quad (1)$$

3.2. Ground Observations Data Processing for Mineral Analysis

Rice (2022), conducted a study using calibrated Mastcam observations to radiance using pre-flight calibration coefficients from radiance products available via the NASA Planetary Data System (PDS) (Bell et al., 2017). Because of their work, they has built a comprehensive database of Mastcam spectra that ROIs the diversity observed across the Curiosity rover's traverse, from a total of 624 observations between sols 0-2302.

In their study, Rice (2022) sampled each image in eight different classes: undisturbed soil, disturbed soil; dump pile, drill tailings, DRT target, broken rock, dusty rock, or vein. In their study, they calculated the distances of the ROIs from the rover and determined the formation and members of each ROI. Additionally, it has been classified into two parts as in-place or float for rocks. In this study, all points in the VRR (sol 1800 – sol 2300) were identified, including dusty rock and in-place in Rice (2022) database. The images of the detected ROIs were examined one by one and reviewed for the second time on the basis of bedrock.

The ROI coordinates have been produced in order to more closely match CRISM pixels. The equation was created using the extracted ROI coordinates, the rover coordinate, the rover distance estimated by Rice (2022) in the database, and the azimuth angles in the "*.lbl" files retrieved from the Curiosity (MSL) Analyst's Notebook (https://an.rsl.wustl.edu/msl/mslbrowser/an3.aspx) site.

The indice values of the ROIs whose coordinates were calculated were calculated in accordance with the methodology outlined by Bell et al. (2000), as detailed in Equation 5. In Equation 2, the value of a is 0.556, while the value of b is 0.444.

$$BD867 = 1 - \left(\frac{R_{867}}{a * R_{751} + b * R_{1012}}\right) \quad (2)$$

3.3. Relationship Between Ground Observations and Remote Sensing

The relationship between the BD860_2 indice, which calculates the band depth at 860 nm, where the hematite is absorbed in the Mastcam sensor, and the BD867 indice, which calculates the band depth at 867 nm, where the hematite is absorbed, in CRISM data, has been examined on the basis of members. The location of 38 CRISM pixels corresponding to the ROIs calculated with the BD867 indice from the Mastcam sensor is shown in Figure 7.

Statistical methods were used to determine whether the model established between CRISM and Mastcam data is acceptable. The r statistic, ME, MAE, NSE, and PB comparison statistics were used to analyze the model results. The formulas with which these statistics were calculated are given in Table 3.

The r statistic, ME, MAE, NSE, and PB were employed as comparative statistics (Table 3). The r statistic is used to assess the quality of fit of a linear relationship and has an optimal value of one. The NSE, which ranges from minus infinity to +1, with a value of +1 indicating a perfect fit, is a measure of the relative size of the variance of the residuals compared to the variance of the observations (Nash and Sutcliffe, 1970). The ME determines whether the CRISM and

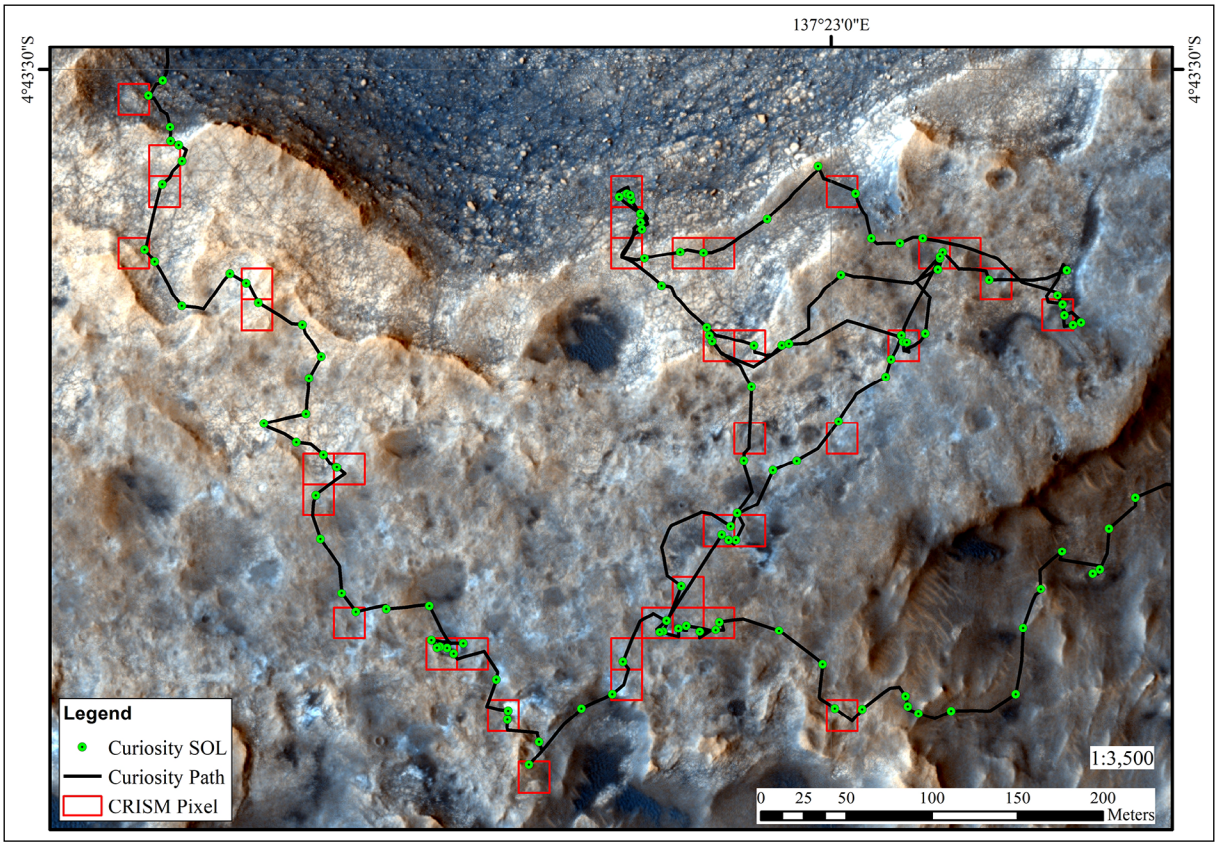

Figure 7- Investigated CRISM pixels and Curiosity rover path.

Table 3- Comparative statistics formulas.

Name	Formula
Pearson Correlation Coefficient	$r = \frac{\sum_{i=1}^{N} (G_i - \bar{G})(C_i - C')}{\sqrt{(G_i - \bar{G})^2}\sqrt{(C_i - C')^2}}$
Mean Error	$ME = \frac{1}{N}\sum_{i=1}^{N} (C_i - G_i)$
Mean Absolute Error	$MAE = \frac{1}{N}\sum_{i=1}^{N} (\lvert C_i - G_i \rvert)$
Nash-Sutcliffe Efficiency Coefficient	$NSE = 1 - \frac{\sum_{i=1}^{N} (C_i - G_i)^2}{\sum_{i=1}^{N} (G_i - \bar{G})^2}$
Percent Bias	$PB = 100\frac{\sum_{i=1}^{N} (C_i - G_i)}{\sum_{i=1}^{N} G_i}$

G_i=Mastcam observations, $\bar{G}$ = Average Mastcam observations, C_i= CRISM estimations, C' = Average CRISM estimations and N=number of data pairs.

point-based estimates are over- or underestimated, while the MAE indicates the average size of the absolute error. The ideal value for both is zero. The PB computes the difference between observed and predicted values and has an ideal value of zero.

4. Results and Discussion

Hematite on Mars is prevalent as a nanophase powder, with crystals sized at the nanometer scale. Fine-grained (red) and coarse-grained (gray) hematite generate stronger absorptions around 0.5 and 0.9 µm wavelengths due to iron-induced charge transfer and crystal field transitions (The MICA Files, 2019). The wavelength graph and absorption values of the hematite mineral in the Minerals Identified through CRISM Analysis (MICA) archive are presented in Figure 8.

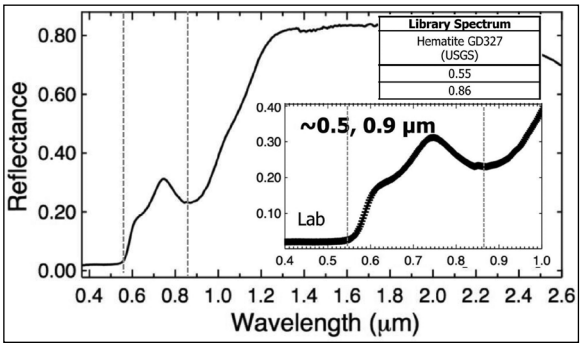

Figure 8- Hematite mineral wavelength (The MICA Files, 2019)

The BD860_2, which calculates the band depth of 0.860 µm wavelength, where the hematite mineral is highly absorbed, was calculated separately for each pixel of the CRISM data, which has a spatial resolution of 18 m, with the help of the formula given in Equation 1. Because of the calculations, the values of the BD860_2 indice in the study area were found to be between -0.016 and 0.018, and the produced hematite mineral distribution map is given in Figure 9.

While composite parameters such as particle size and albedo exert an influence on the band depth, the relationship is generally proportional to the amount of the absorbed material (Clark and Roush, 1984; Pelkey et al., 2007). When the distribution map of the hematite mineral given in Figure 9 is examined, it is seen that the hematite is more abundant in the northwest and northeast regions of the study area compared to the other regions. In the 500-day period from Sol 1800 to Sol 2300 covering the study area, the points where Mastcam BD867 was calculated were determined one by one and the map we produced is shown in Figure 10.

It was observed that 72 sol points detected hit 38 CRISM pixel; more than one indice were calculated for each sol point, and it was determined that more than one sol point fell on each CRISM pixel. The

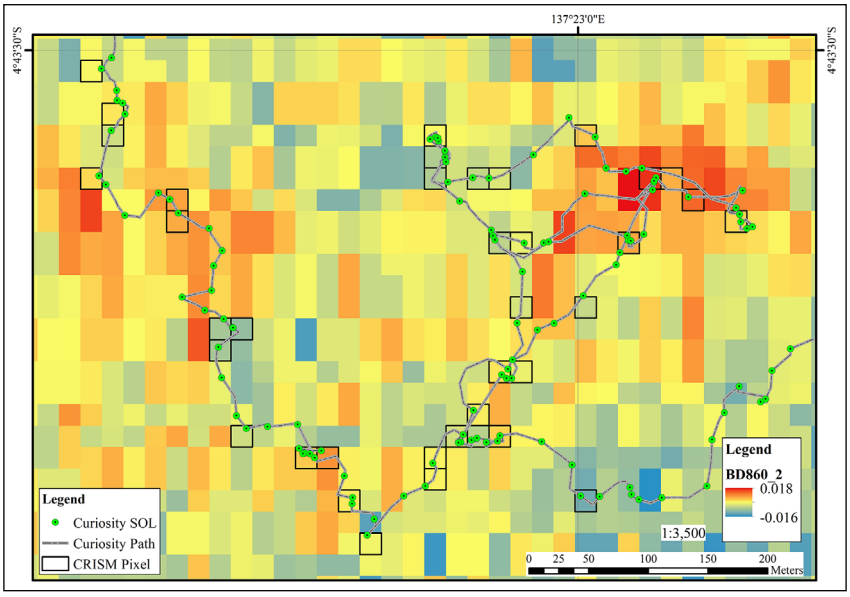

Figure 9- Hematite mineral distribution map produced using CRISM (Akgül and Ural, 2022).

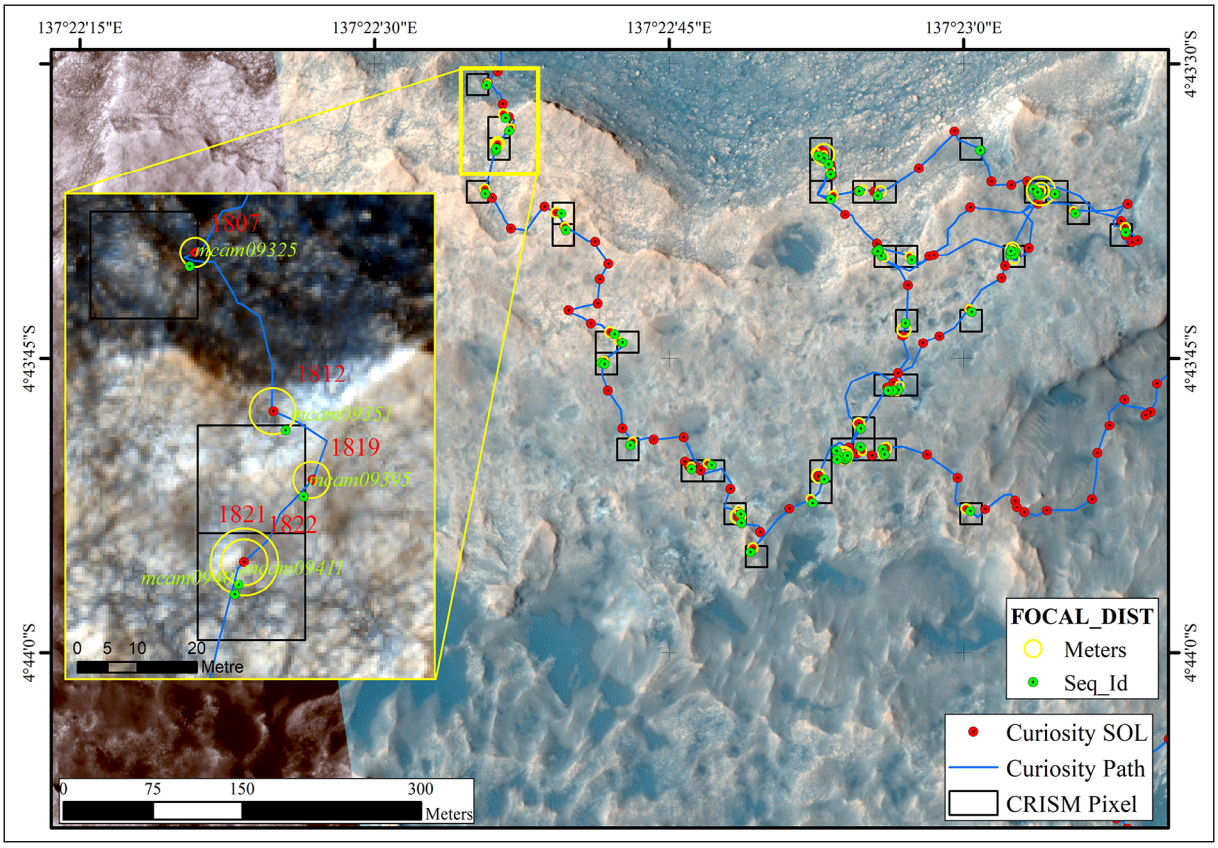

Figure 10- Investigated CRISM pixels and Curiosity rover route.

Mastcam BD867 Indice ROIs corresponding to each CRISM pixel were grouped independently of the sol day, and their descriptive statistical values were calculated using the formulas shown in Table 3. The r statistic, ME, MAE, NSE, and PB statistics were calculated for all points as calculated for members of BP, PP, and JR (Table 4).

When the values of the r statistic are examined in the statistical results, it is seen that there is a strong relationship for the values of all points, and a very strong relationship for the values of the PP member (Cohen, 1988; Sabilla et al., 2019). When the ME and MAE values, which should approach 0 for a perfect fit, are examined, it is seen that JR and BP members get the best results. When the statistical results of the NSE, which is acceptable with values greater than 0, and the PB with the optimal value of 0, are examined, it is seen that the JR member has the best result.

Rampe et al., 2020, analyzed the drilling samples they took from BP, PP and JR members in their study using the Chemin detector, and they found the amount of hematite in the samples as a percentage to be 6.1% for BP, 14.7% for PP and 2.9% and 8.5% for JR. When the r statistics given in Table 4 are examined, it is seen that our study is parallel to the study of Rampe et al. (2020). PP member (r:70%, wt:14.7%) got the

Table 4- Performance statistics.

Member	r	ME	MAE	NSE	PB (%)	Number of Points
Blunts Point (BP)	-0.20	-0.003	0.010	-0.24	-440.45	7
Pettegrove Point (PP)	**0.70**	-0.020	0.025	-0.18	-76.15	43
Jura (JR)	0.13	0.001	0.019	0.01	-49.14	34
All points	0.66	-0.010	0.021	0.15	-79.98	84

highest value in both studies, then JR member (r:13%, wt:8.5%), and finally BP member (r:-20%) , wt: 6.1%).

The CRISM BD860_2 graph drawn against Mastcam BD867 belonging to all members without distinction of BP, PP, and JR members in the VRR region is given in Figure 11.

Although Viviano-Beck et al. (2014) stated in Equation 1 how to calculate the BD860_2 indice in their study, a new hematite mineral sensitive indice, which we named ModBD860_2, was sensitized by ground observations by integrating the formula they gave and the regression coefficients of the appropriate value we found in Figure 11 (Equation 3).

$$ModBD860\_2 = 2.6581 - \left(\frac{2.6522 * R_{860}}{0.527 * R_{755} - 0.473 * R_{977}}\right) \quad (3)$$

In this equation, it is possible to reach the hematite distribution, which is the sensitivity reached by the Mastcam sensor in ground observations, by substituting the reflectance values of the CRISM data at 755 nm, 860 nm and 977 nm wavelengths.

5. Conclusion

The Curiosity rover conducted an extensive investigation of the VRR region, a topographical ridge extending northeast-southwest on the northwest slope of Aeolis Mons, for approximately seventeen months. This investigation represents the longest and most comprehensive exploration of Mars' lacustrine layers to date. The mineral hematite, which is sensitive to 860 nm band depth in CRISM data from the MRO satellite and 867 nm band depth in the Mastcam sensor on the Curiosity rover, was discovered in the VRR region through the use of both the CRISM and Mastcam sensors.

To determine the adjustment to be applied to the CRISM data, a model was created using 84 Mastcam ROIs, which corresponded to 38 CRISM pixels in the research region. The BD860_2 indice defining the hematite mineral was modified as ModBD860_2 by applying the regression coefficients of the model with an r statistic of 66% and a MAE value of 2.1%.

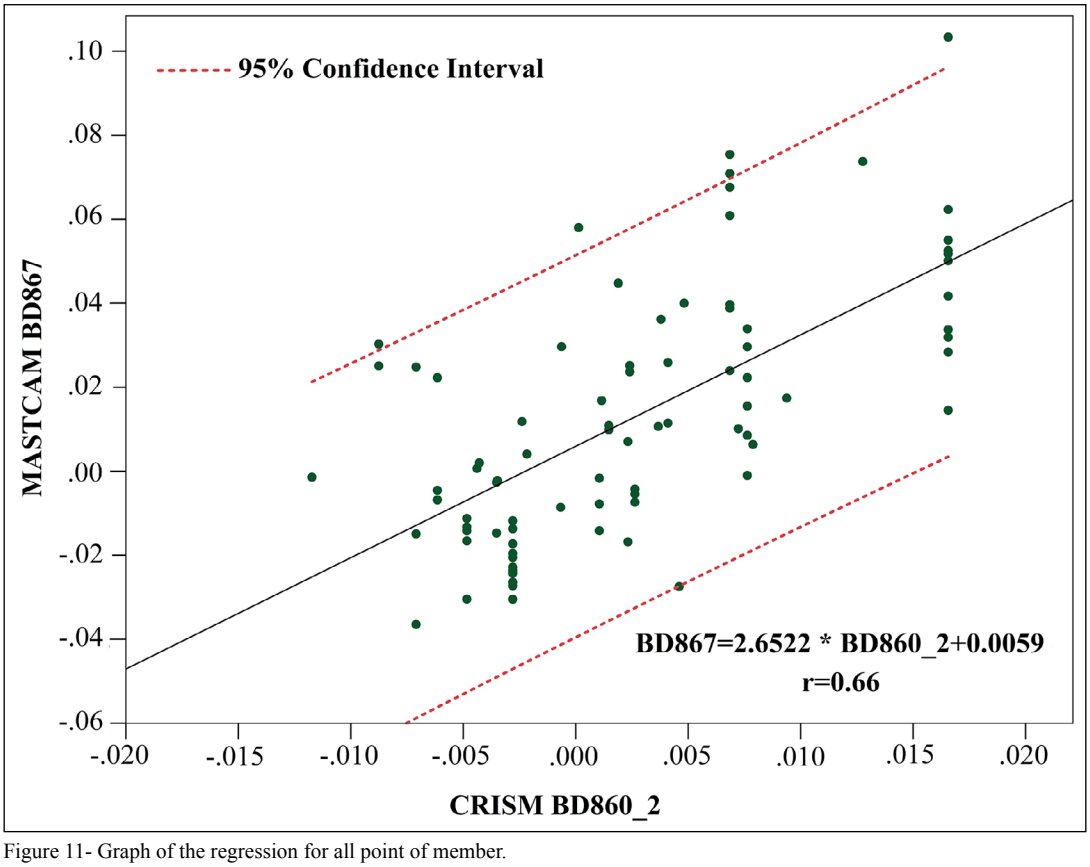

Figure 11- Graph of the regression for all point of member.

It has been demonstrated that places where satellite data cannot detect the existence of hematite using present methodologies can also be prospective research topics by applying the algorithm created within the scope of this study to CRISM data. It was concluded that CRISM data using corrected indices such as ModBD860_2 indice would be more accurate in planning the location of the landing craft or the route planning of the rovers to find important minerals such as hematite in the future.

The VRR region contains three distinct members: BP, PP, and JR. An investigation was conducted into the relationship between the CRISM pixels corresponding to each member and the Mastcam ROIs. Upon examining the values of the r statistic in the statistical results, it was observed that there is a strong relationship for the values of all points and a very strong relationship for the values of the PP member. When the mean error (ME) and the mean absolute error (MAE) values, which are expected to approach 0 for an ideal fit, are analyzed, it is observed that the JR and BP members achieve the most optimal results. When the statistical outcomes of the normalized standard error (NSE), which is considered acceptable when greater than 0, and the PB, which attains the optimal value of 0, are examined, it is evident that the JR member yields the most favorable result. For BP, PP, and JR members, the observed values were -20%, 70%, and 13%, respectively. Based on satellite data, the PP member was identified as the primary member of the VRR region, which was determined to be the hematite ridge.

Acknowledgement

The remote sensing analyzes used in this study was prepared by benefiting from the PhD Thesis titled “Investigation of Hematite Mineral Distribution by Remote Sensing and Ground Observations in Mars/ Gale Crater” conducted by Mehmet Ali Akgül.

References

Akgül, M. A., Ural, S. 2022. Mineralogical Mapping on Mars Using Hyperspectral CRISM Data. Geosound 55 (1), 1-19.

Arvidson, R., Morgan, F., Seelos, F., Seelos, K. 2017. Crism demonstration: Data access, processing, and analysis. Flagstaff, Arizona, ABD. 3rd Planetary Data Workshop.

Bell, J. F. III., Mcsween, H. Y., Crisp, J. A., Morris, R. V., Murchie, S. L., Bridges, N. T., Johnson, J. R., Britt, D. T., Golombek, M. P., Moore, H. J., Ghosh, A., Bishop, J. L., Anderson, R. C., Brückner, J., Economou, T., Greenwood, J. P., Gunnlaugsson, H. P., Hargraves, R. M., Hviid, S., Knudsen, J. M., Madsen, M. B., Reid, R., Rieder, R., Soderblom, L. 2000. Mineralogic and compositional properties of Martian soil and dust: results from Mars Pathfinder. Journal of Geophysical Research: Planets 105, 1721–1755.

Bell, J. F. III., Godber, A., McNair, S., Caplinger, M. A., Maki, J. N., Lemmon, M. T., Van Beek, J., Malin, M. C., Wellington, D., Kinch, K. M., Madsen, M. B., Hardgrove, C., Ravine, M. A., Jensen, E., Harker, D., Anderson, R. B., Herkenhoff, K. E., Morris, R. V., Cisneros, E., Deen, R. G. 2017. The Mars Science Laboratory Curiosity Rover Mastcam instruments: Preflight and in-flight calibration, validation, and data archiving. Earth and Space Science 4, 396–452.

Bennett, K. A., Rivera-Hernández, F., Tinker, C., Horgan, B., Fey, D. M., Edwards, C., Edgar, L. A., Kronyak, R., Edgett, K. S., Fraeman, A., Kah, L. C., Henderson, M., Stein, N., Dehouck, E., Williams, A. J. 2021. Diagenesis Revealed by Fine-Scale Features at Vera Rubin Ridge, Gale Crater, Mars. Journal of Geophysical Research: Planets 126(5), 1-24.

Bibring, J. P., Langevin, Y., Mustard, J.F., Poulet, F., Arvidson, R., Gendrin, A., Gondet, B., Mangold, N., Pinet. P,, Forget, F., Berthé, M., Bibring, J.P., Gendrin, A., Gomez, C., Gondet, B., Jouglet, D., Poulet, F., Soufflot, A., Vincendon, M., Combes, M., Drossart, P., Encrenaz, T., Fouchet, T., Merchiorri, R., Belluci, G., Altieri, F., Formisano, V., Capaccioni, F., Cerroni, P., Coradini, A., Fonti, S., Korablev, O., Kottsov, V., Ignatiev, N., Moroz, V., Titov, D., Zasova, L., Loiseau, D., Mangold, N., Pinet, P., Douté, S., Schmitt, B., Sotin, C., Hauber, E., Hoffmann, H., Jaumann, R., Keller, U., Arvidson, R., Mustard, J.F., Duxbury, T., Forget, F., Neukum, G. 2006. Global mineralogical and aqueous mars history derived from OMEGA/ Mars Express data. Science 312(5772), 400-404.

Bibring, J. P., Arvidson, R. E., Gendrin, A., Gondet, B., Langevin, Y., Le Mouelic, S., Mangold, N., Morris, R. V., Mustard, J. F., Poulet, F., Quantin, C., Sotin, C. 2007. Coupled Ferric Oxides and Sulfates on the Martian Surface. Science 317, 1206–1210.

Bristow, T. F., Rampe, E. B., Achilles, C. N., Blake, D. F., Chipera, S. J., Craig, P., Crisp, J. A., Des Marais, D. J., Downs, R. T., Gellert, R., Grotzinger, J. P., Gupta, S., Hazen, R. M., Horgan, B., Hogancamp, J. V., Mangold, N., Mahaffy, P. R., McAdam, A. C., Ming, D. W., Morookian, J. M., Morris, R. V., Morrison, S. M., Treiman, A. H., Vaniman, D. T., Vasavada, A. R., Yen, A. S. 2018. Clay mineral diversity and abundance in sedimentary rocks of Gale crater, Mars. Science Advances 4(6), eaar3330.

Buz, J., Ehlmann, B. L., Pan, L., Grotzinger, J. P. 2017. Mineralogy and stratigraphy of the Gale crater rim, wall, and floor units. Journal of Geophysical Research: Planets 122, 1090– 1118.

Clark, R. N., Roush, T. L. 1984. Reflectance spectroscopy: Quantitative analysis techniques for remote sensing applications, Journal of Geophysical Research: Planets 89(B7), 6329.

Cohen, J. 1988. Statistical Power Analysis for the Behavioral Sciences (2nd ed.). Hillside, NJ: Lawrence Erlbaum Associates.

Edgar, L. A., Fedo, C. M., Gupta, S., Banham, S. G., Fraeman, A. A., Grotzinger, J. P., Stack, K. M., Stein, N. T., Bennett, K. A., Rivera-Hernández, F., Sun, V. Z., Edgett, K. S., Rubin, D. M., House, C., Van Beek, J. 2020. A Lacustrine Paleoenvironment Recorded at Vera RubinRidge, Gale Crater: Overview of the Sedimentology and Stratigraphy Observed by the Mars ScienceLaboratory Curiosity Rover. Journal of Geophysical Research: Planets 125(3).

Eng, A. M., Rice, M. S., Farrand, W. H., Johnson, J. R., Jacob, S., Rampe, E. B., Thompson, L., St. Clair, M., Applin, D., Bishop, J., Cloutis, E., Gabbert, M., Haber, James T., Lapo, K., Rudolph, A., Seeger, C., Sheppard, R. 2024. A Mastcam multispectral investigation of rock variability in Gale crater, Mars: Implications for alteration in the clay-sulfate transition of Mount Sharp. Journal of Geophysical Research: Planets 129, e2023JE008033.

ESA 2025. https://www.esa.int/Science_Exploration/Human_and_Robotic_Exploration/Exploration/ExoMars. Date of access: 18.02.2025.

Fedo, C., Grotzinger, J. P., Gupta, S., Fraeman, A., Edgar, L., Edgett, K., Stein, N., Rivera-Hernandez, F., Lewis, K., Stack, K. M., House, C., Rubin, D., Vasavada, A. R. 2018. Sedimentology and stratigraphy of the Murray formation, Gale Crater, Mars. LPSC 49, 2078.

Fedo, C. M., Grotzinger, J. P., Gupta, S., Banham, S., Bennett, K., Edgar, L., Fox, V., Fraeman, A., House, C., Lewis, K., Stack, K. M., Rubin, D., Siebach, K., Sumner, D., Sun, V., Vasavada, A. 2019. Evidence for persistent, water-rich, lacustrine deposition preserved in the Murray formation, Gale crater: A depositional system suitable for sustained habitability. Ninth International Conference on Mars, 6308.

Fraeman, A. A., Arvidson, R. E., Catalano, J. G., Grotzinger, J. P., Morris, R. V., Murchie, S. L., Stack, K. M., Humm, D. C., McGovern, J. A., Seelos, F. P., Seelos, K. D., Viviano, C. E. 2013. A hematite-bearing layer in Gale Crater, Mars: Mapping and implications for past aqueous conditions. Geology 41(10), 1103–1106.

Fraeman, A. A., Ehlmann, B. L., Arvidson, R. E., Edwards, C. S., Grotzinger, J. P., Milliken, R. E., Quinn, D. P., Rice, M. S. 2016. The stratigraphy and evolution of lower Mount Sharp from spectral, morphological, and thermophysical orbital data sets. Journal of Geophysical Research: Planets 121(9), 1713–1736.

Fraeman, A. A., Johnson, J. R., Arvidson, R. E., Rice, M. S., Wellington, D. F., Morris, R. V., Fox, V. K., Horgan, B. H. N., Jacob, S. R., Salvatore, M. R., Sun, V. Z., Pinet, P., Bell, J. F., Wiens, R. C., Vasavada, A. R. 2020. Synergistic ground and orbital observations of iron oxides on Mt. Sharp and Vera Rubin ridge. Journal of Geophysical Research: Planets 125, e2019JE006294.

Golombek, M. P., Grant, J. A., Crumpler, L. S., Greeley, R., Arvidson, R. E., Bell III, J. F., Weitz, C. M., Sullivan, R., Christensen, P. R., Soderblom, L. A., Squyres, S. W. 2006. Erosion rates at the Mars Exploration Rover landing sites and long-term climate change on Mars. Journal of Geophysical Research 111(E12).

Golombek, M., Grant, J., Kipp, D., Vasavada, A., Kirk, R., Fergason, R., Bellutta, P., Calef, F., Larsen, K., Katayama, Y., Huertas, A., Beyer, R., Chen, A., Parker, T., Pollard, B., Lee, S., Sun, Y., Hoover, R., Sladek, H., Grotzinger, J., Welch, R., Noe Dobrea, E., Michalski, J., Watkins, M. 2012. Selection of the Mars Science Laboratory Landing Site. Space Science Reviews 170(1), 641–737.

Grant, J. A., Wilson, S. A. 2011. Late alluvial fan formation in southern Margaritifer Terra, Mars. Geophysical Research Letters 38, no. L08201.

Grotzinger, J. P., Crisp, J., Gellert, R., Gilbert, J. B., Golombek, M., Gomez-elvira, J., Hassler, D. M., Jandura, L., Litvak, M., Mahaffy, P., Maki, J., Meyer, M., Vasavada, A. R., Malin, M. C., Mitrofanov, I., Simmonds, J. J., Vaniman, D., Welch, R. V., Wiens, R. C., Anderson, R. C.,

Baker, C. J., Barry, R., Blake, D. F., Conrad, P., Edgett, K. S., Ferdowski, B. 2012. Mars Science Laboratory Mission and Science Investigation. Space Science Reviews 170(1), 5–56.

Grotzinger, J. P., Sumner, D. Y., Kah, L. C., Stack, K., Gupta, S., Edgar, L., Rubin, D., Lewis, K., Schieber, J., Mangold, N., Milliken, R., Conrad, P. G., DesMarais, D., Farmer, J., Siebach, K., Calef, F., Hurowitz, J., McLennan, S. M., Ming, D., Vaniman, D., Crisp, J., Vasavada, A., Edgett, K. S., Malin, M., Blake, D., Gellert, R., Mahaffy, P., Wiens, R. C., Maurice, S., Grant, J. A., Wilson, S., Anderson, R. C., Beegle, L., Arvidson, R., Hallet, B., Sletten, R. S., Rice, M., Bell, J., Griffes, J., Ehlmann, B., Anderson, R. B., Bristow, T. F., Dietrich, W. E., Dromart, G., Eigenbrode, J., Fraeman, A., Hardgrove, C., Herkenhoff, K., Jandura, L., Kocurek, G., Lee, S., Leshin, L. A., Leveille, R., Limonadi, D., Maki, J., McCloskey, S., Meyer, M., Minitti, M., Newsom, H., Oehler, D., Okon, A., Palucis, M., Parker, T., Rowland, S., Schmidt, M., Squyres, S., Steele, A., Stolper, E., Summons, R., Treiman, A., Williams, R., Yingst, A. 2014. A Habitable Fluvio-Lacustrine Environment at Yellowknife Bay, Gale Crater, Mars. Science 343(6169),1-14.

Grotzinger, J. P., Gupta, S., Malin, M. C., Rubin, D. M., Schieber, J., Siebach, K., Sumner, D. Y., Stack, K. M., Vasavada, A. R., Arvidson, R. E., Calef, F., Edgar, L., Fischer, W. F., Grant, J. A., Griffes, J., Kah, L. C., Lamb, M. P., Lewis, K. W., Mangold, N., Minitti, M. E., Palucis, M., Rice, M., Williams, R. M. E., Yingst, R. A., Blake, D., Blaney, D., Conrad, P., Crisp, J., Dietrich, W. E., Dromart, G., Edgett, K. S., Ewing, R. C., Gellert, R., Hurowitz, J. A., Kocurek, G., Mahaffy, P., McBride, M. J., McLennan, S. M., Mischna, M., Ming, D., Milliken, R., Newsom, H., Oehler, D., Parker, T. J., Vaniman, D., Wiens, R. C., Wilson, S. A. 2015. Deposition, exhumation, and paleoclimate of an ancient lake deposit, Gale crater, Mars. Science 350(6257), aac7575.

Gurunadham, R., Kumar, S. 2014. Extraction of aqueous minerals on Mars using CRISM based Targeted Reduced Data Records. International Archives of the Photogrammetry. Remote Sensing and Spatial Information Sciences XL-8, 431–436.

Gwizd, S., Fedo, C., Grotzinger, J., Edgett, K., Rivera-Hernandez, F., Stein, N. 2019. Depositional history of the Hartmann's Valley member, Murray formation, Gale crater, Mars. 49th Lunar and Planetary Science Conference, 19–23 March 2018, Texas, USA, Abstract 2150.

Hartmann, W. K., Neukum, G. 2001. Cratering Chronology and the Evolution of Mars. Space Science Reviews 96, 165–194.

Horgan, B. H. N., Johnson, J. R., Fraeman, A. A., Rice, M. S., Seeger, C., Bell, J. F., 3rd, Bennett, K. A., Cloutis, E. A., Edgar, L. A., Frydenvang, J., Grotzinger, J. P., L'Haridon, J., Jacob, S. R., Mangold, N., Rampe, E. B., Rivera-Hernandez, F., Sun, V. Z., Thompson, L. M., Wellington, D. 2020. Diagenesis of Vera Rubin Ridge, Gale Crater, Mars, From Mastcam Multispectral Images. Journal of Geophysical Research: Planets 125(11), e2019JE006322.

Hurowitz, J. A., Grotzinger, J. P., Fischer, W. W., McLennan, S. M., Milliken, R. E., Stein, N., Vasavada, A. R., Blake, D. F., Dehouck, E., Eigenbrode, J. L., Fairén, A. G., Frydenvang, J., Gellert, R., Grant, J. A., Gupta, S., Herkenhoff, K. E., Ming, D. W., Rampe, E. B., Schmidt, M. E., Siebach, K. L., Stack-Morgan, K., Sumner, D. Y., Wiens, R. C. 2017. Redox stratification of an ancient lake in Gale crater, Mars. Science 356(6341), eaah6849.

Jacob, S. R., Wellington, D. F., Bell, J. F., Achilles, C., Fraeman, A. A., Horgan, B., Johnson, J. R., Maurice, S., Peters, G. H., Rampe, E. B., Thompson, L. M., Wiens, R. C. 2020. Spectral, compositional, and physical properties of the Upper Murray formation and Vera Rubin ridge, Gale crater, Mars. Journal of Geophysical Research: Planets 125, e2019JE006290.

Milliken, R. E., Grotzinger, J. P., Thomson, B. J. 2010. Paleoclimate of Mars as captured by the stratigraphic record in Gale crater. Geophysical Research Letters 37, L04201.

Morgan, M. F., Seelos, F. P., Murchie, S. L. 2017. The CRISM Analysis Toolkit (CAT): Overview and Recent Updates. 3rd Planetary Data Workshop, The Planetary Geologic Mappers Annual Meeting, 12–15 June 2017, Arizona, USA.

Murchie, S., Arvidson, R., Bedini, P., Beisser, K., Bibring, J. P., Bishop, J., Boldt, J., Cavender, P., Choo, T., Clancy, R. T., Darlington, E. H., Des Marais, D., Espiritu, R., Fort, D., Green, R., Guinness, E., Hayes, J., Hash, C., Heffernan, K., Hemmler, J., Heyler, G., Humm, D., Hutcheson, J., Izenberg, N., Lee, R., Lees, J., Lohr, D., Malaret, E., Martin, T., McGovern, J. A., McGuire, P., Morris, R., Mustard, J., Pelkey, S., Rhodes, E., Robinson, M., Roush, T., Schaefer, E., Seagrave, G., Seelos, F., Silverglate, P., Slavney, S., Smith, M., Shyong, W.J., Strohbehn, K., Taylor, H., Thompson, P., Tossman, B., Wirzburger, M., Wolff, M. 2007.

Compact Connaissance Imaging Spectrometer for Mars (CRISM) on Mars Reconnaissance Orbiter (MRO). J. Geophys. Res. Planets 112.

Nash J. E., Sutcliffe J. V. 1970. River flow forecasting through conceptual models part I — A discussion of principles. Journal of Hydrology 10(3), 282–290.

Pelkey, S. M., Mustard, J. F., Murchie, S., Clancy, R. T., Wolff, M., Smith, M., Milliken, R., Bibring, J.-P., Gendrin, A., Poulet, F., Langevin, Y., Gondet, B. 2007. CRISM multispectral summary products: Parameterizing mineral diversity on Mars from reflectance. Journal of Geophysical Research: Planets 112(E8), E08S14-n/a.

Rampe, E. B., Ming, D. W., Blake, D. F., Bristow, T. F., Chipera, S. J., Grotzinger, J. P., Morris, R. V., Morrison, S. M., Vaniman, D. T., Yen, A. S., Achilles, C. N., Craig, P. I., Des Marais, D. J., Downs, R. T., Farmer, J. D., Fendrich, K. V., Gellert, R., Hazen, R. M., Kah, L. C., Morookian, J. M., Peretyazhko, T. S., Sarrazin, P., Treiman, A. H., Berger, J. A., Eigenbrode, J., Fairén, A. G., Forni, O., Gupta, S., Hurowitz, J. A., Lanza, N. L., Schmidt, M. E., Siebach, K., Sutter, B., Thompson, L. M. 2017. Mineralogy of an ancient lacustrine mudstone succession from the Murray formation, Gale crater, Mars. Earth and Planetary Science Letters 471, 172–185.

Rampe, E. B., Bristow, T. F., Morris, R. V., Morrison, S. M., Achilles, C. N., Ming, D. W., Vaniman, D. T., Blake, D. F., Tu, V. M., Chipera, S. J., Yen, A. S., Peretyazhko, T. S., Downs, R. T., Hazen, R. M., Treiman, A. H., Grotzinger, J. P., Castle, N., Craig, P. I., Marais, D. J. Des, Thorpe, M. T., Walroth, R. C., Downs, G. W., Fraeman, A. A., Siebach, K. L., Gellert, R., Lafuente, B., McAdam, A. C., Meslin, P.-Y., Sutter, B., Salvatore, M. R. 2020. Mineralogy of Vera Rubin ridge from the Mars Science Laboratory CheMin instrument. Journal of Geophysical Research: Planets 125, e2019JE006306.

Rapin, W., Ehlmann, B. L., Dromart, G., Schieber, J., Thomas, N. H., Fischer, W. W., Fox, V. K., Stein, N. T., Nachon, M., Clark, B. C., Kah, L. C., Thompson, L., Meyer, H. A., Gabriel, T. S. J., Hardgrove, C., Mangold, N., Rivera-Hernandez, F., Wiens, R. C., Vasavada, A. R. 2019. An interval of high salinity in ancient Gale crater lake on Mars. Nature Geoscience 12(11), 889–895.

Rice, M. S. 2022. Mastcam multispectral database from the Curiosity rover's traverse in Gale crater, Mars (sols 0-2302). Geology Faculty Publications 104.

Rice, M. S., Seeger, C., Bell, J., Calef, F., St. Clair, M., Eng, A., Fraeman, A. A., Hughes, C., Horgan, Briony., Jacob, S., Johnson, J., Kerner, H., Kinch, K., Lemmon, M., Million, C., Starr, M., Wellington, D. 2022. Spectral diversity of rocks and soils in Mastcam observations along the Curiosity rover's traverse in Gale crater, Mars. Journal of Geophysical Research: Planets 127, e2021JE007134.

Rivera-Hernandez, F., Sumner, D. Y., Mangold, N., Banham, S. G., Edgett, K. S., Fedo, C. M., Gupta, S., Gwizd, S., Heydari, E., Maurice, S., Nachon, M., Newsom, H., Schieber, J., Stack-Morgan, K., Stein, N., Wiens, R. C. 2020. Grain size variations in the Murray formation: Stratigraphicevidence for changing depositional environments in Gale crater, Mars. Journal of Geophysical Research: Planets 125, e2019JE006230.

Seelos, F. P., Seelos, K. D., Murchie, S. L., Novak, M. A. M., Hash, C. D., Morgan, M. F., Arvidson, R. E., Aiello, J., Bibring, J., Bishop, J. L., Boldt, J. D., Boyd, A. R., Buczkowski, D. L., Chen, P. Y., Clancy, R. T., Ehlmann, B. L., Frizzell, K., Hancock, K. M., Hayes, J. R., Heffernan, K. J., Humm, D. C., Itoh, Y., Ju, M., Kochte, M. C., Malaret, E., McGovern, J. A., McGuire, P., Mehta, N. L., Moreland, E. L., Mustard, J. F., Nair, A. H., Núnez., J. I., O'Sullivan, J. A., Packer, L. L., Poffenbarger, R. T., Poulet, F., Romeo, G., Santo, A. G., Smith, M. D., Stephens, D. C., Toigo, A. D., Viviano, C. E., Wolff, M. J. 2024. The CRISM investigation in Mars orbit: Overview, history, and delivered data products. Icarus 419, 115612.

Sabilla, S. I., Sarno, R., Triyana, K. 2019. Optimizing threshold using pearson correlation for selecting features of electronic nose signals. International Journal of Intelligent Engineering and Systems 12(6), 81-90.

Stack, K. E., Sun, V. Z., Arvidson, R. E., Fedo, C., Day, M., Bennett, K., Edgar, L. A., Fox, V. K., Cofield, S. 2019. Origin of linear ridges in the clay-bearing unit of Mount Sharp, Gale Crater, Mars. 50th Lunar and Planetary Science Conference, 18–22 March 2019, Texas, USA, 1210.

Stein, N., Grotzinger, J. P., Schieber, J., Mangold, N., Hallet, B., Newsom, H., Stack, K. M., Berger, J. A., Thompson, L., Siebach, K. L., Cousin, A., le Mouélic, S., Minitti, M., Sumner, D. Y., Fedo, C., House, C. H., Gupta, S., Vasavada, A. R., Gellert, R., Wiens, R. C., Frydenvang, J., Forni, O., Meslin, P. Y., Payré, V., Dehouck, E. 2018. Desiccation cracks provide evidence of lake

drying on Mars, Sutton Island member, Murray formation, Gale Crater. Geology 46(6), 515–518.

Stein, N. T., Quinn, D. P., Grotzinger, J. P., Fedo, C., Ehlmann, B. L., Stack, K. M., Edgar, L. A., Fraeman, A. A., Deen, R. 2020. Regional structural orientation of the Mount Sharp group revealed by in situ dip measurements and stratigraphic correlations on the Vera Rubin ridge. Journal of Geophysical Research: Planets 125, e2019JE006298.

Tanaka, K. L., Skinner, J. A., Jr., Dohm, J. M., Irwin, R. P., III, Kolb, E. J., Fortezzo, C. M., Platz, T., Michael, G. G., Hare, T. M. 2014. Geologic Map of Mars: U.S. Geological Survey Scientific Investigations Map 3292, scale 1:20,000,000, pamphlet 43.

The MICA Files, 2019. Minerals Identified through CRISM Analysis, Assembled by the CRISM Science Operations Center, Johns Hopkins University Applied Physics Laboratory, 104.

Tinker, C. R., Horgan, B., Bennett, K. 2019. Morphology and occurrence of dark toned diagenetic features in the Vera Rubin ridge, Gale crater, Mars from MAHLI color images, 50th Lunar and Planetary Science Conference, 18–22 March 2019, Texas, USA, Abstract 1730.

Turner, M., Lewis, K. 2023. Geologic structure of the Vera Rubin ridge, Gale crater, Mars. Journal of Geophysical Research: Planets 128, e2022JE007237.

Vasavada, A. R., Grotzinger, J. P., Arvidson, R. E., Calef, F. J., Crisp, J. A., Gupta, S., Hurowitz, J., Mangold, N., Maurice, S., Schmidt, M. E., Wiens, R. C., Williams, R. M. E., Yingst, R. A. 2014. Overview of the Mars Science Laboratory mission: Bradbury Landing to Yellowknife Bay and beyond. Journal of Geophysical Research: Planets 119, 1134–1161.

Viviano-Beck, C. E., Seelos, F. P., Murchie, S. L., Kahn, E. G., Seelos, K. D., Taylor, H. W., Taylor, K., Ehlmann, B. L., Wisemann, S. M., Mustard, J. F., Morgan, M. F. 2014. Revised CRISM spectral parameters and summary products based on the currently detected mineral diversity on Mars. Journal of Geophysical Research: Planets 119, 1403–1431.

Wray, J. J. 2013. Gale crater: The Mars Science Laboratory/ Curiosity rover landing site. International Journal of Astrobiology 12(1), 25–38.

Xue, Y., Jin, S. 2014. Martian Minerals and Rock Components from MRO CRISM Hyperspectral Images. Planetary Geodesy and Remote Sensing. CRC Press Taylor & Francis Group 6000 Broken Sound Parkway NW, Suite 300 Boca Raton, FL, USA.